Controlled Light–Matter Interaction in Graphene Electrooptic Devices Using Nanophotonic Cavities and Waveguides

Xuetao Gan, Ren-Jye Shiue, Yuanda Gao, Solomon Assefa, *Senior Member, IEEE*, James Hone, and Dirk Englund, *Member, IEEE*

(Invited Paper)

***Abstract*—Nanophotonic devices, such as waveguides and cavities, can strongly enhance the interaction of light with graphene. We describe techniques for enhancing the interaction of photons with graphene using chip-integrated nanophotonic devices. Transferring single-layer graphene onto planar photonic crystal nanocavities enables a spectrally selective, order-of-magnitude enhancement of optical coupling with graphene, as shown by spectroscopic studies of cavity modes in visible and infrared spectral ranges. We observed dramatically cavity-enhanced absorption, hot photoluminescence emission, and Raman scattering of the monolayer graphene. We also described a broad-spectrum enhancement of the light–matter interaction by coupling graphene with a bus waveguide on a silicon-on-insulator photonic integrated circuit, which enables a 6.2-dB transmission attenuation due to the graphene absorption over a waveguide length of 70 μm. By electrically gating the graphene monolayer coupled with a planar photonic crystal nanocavity, electrooptic modulation of the cavity reflection was possible with a contrast in excess of 10 dB. Moreover, a novel modulator device based on the cavity-coupled graphene–boron nitride–graphene capacitor was fabricated, showing a modulation speed up to 0.57 GHz. These results indicate the applications of graphene-cavity devices in high-speed and high-contrast modulators with low energy consumption. The integration of graphene with nanophotonic architectures promises a new generation of compact, energy-efficient, and ultrafast electrooptic graphene devices for on-chip optical communications.**

***Index Terms*—Graphene, photonic crystal nanocavity, waveguide, optoelectronics, modulator, photodetector, Raman spectroscopy, photoluminescence (PL).**

I. Introduction

GRAPHENE, a single atomic layer of graphite, has unique electronic properties that result in striking optical phenomena. A strong light–matter interaction results in an elegant expression for the material's absorption coefficient: in visible to near infrared, graphene's absorbance equals $\pi\alpha \approx 2.3\%$, where $\alpha = e^2/\hbar c \approx 1/137$ is the fine-structure constant [1], which can be widely tuned by electrical gating. Combined with its notable electrical transport properties, graphene-based optoelectronics devices, such as ultrafast photodetectors [2], [3] and broadband modulators [4], have been reported recently. A single layer of graphene also displays interesting nonlinear optical phenomena. Due to the relatively low density of states in the infrared, its optical absorption becomes saturable under high-intensity radiation, which enables graphene saturable absorbers for tunable mode-lock lasers [5]. Furthermore, the third-order optical nonlinearity can become important under this strong excitation regime and four-wave mixing with the material has been demonstrated [6]. Although light–graphene interaction is strong given its single atomic thickness, devices relying on single-pass operation are ineffective for either light absorption or strong nonlinear response in photonics applications. Various devices have been developed to enhance the light–graphene interaction, including devices exploiting plasmon [7], [8] or microcavity modes [9], [10] for photodetection. There has also been considerable interest in implementing graphene devices on photonic integrated circuits, including waveguide-integrated modulators [4], [11], photonic crystal nanocavity-based four-wave mixing [12], and modulators [13], [14].

This paper describes the enhanced light–matter interaction in graphene monolayers coupled with planar photonic crystal (PPC) nanocavities and waveguides. In optical cavities, the optical intensity is proportional to Q/V_{mode}, where Q and V_{mode} are the quality factor and mode volume of the resonant mode, respectively. PPC nanocavities can have extremely high Q factor (up to 10^6) and ultrasmall V_{mode} (on the order of a cubic wavelength) [15], which makes them appealing for realizing strong light–matter coupling. This cavity-enhanced coupling can be

Manuscript received April 8, 2013; revised July 3, 2013; accepted July 3, 2013. Date of publication August 7, 2013; date of current version September 23, 2013. This work was supported by the Air Force Office of Scientific Research PECASE, supervised by Dr. G. Pomrenke, and the DARPA Information in a Photon program, under Grant W911NF-10-1-0416. Device fabrication was carried out in part at the Center for Functional Nanomaterials, Brookhaven National Laboratory, which is supported by the U.S. Department of Energy, Office of Basic Energy Sciences, under Contract DE-AC02-98CH10886. The work of X. Gan was supported in part by the 973 program (2012CB921900).

X. Gan is with the School of Science, Northwestern Polytechnical University, Xi'an 710072, China, and also with the Department of Electrical Engineering, Columbia University, NY 10027 USA (e-mail: xuetaogan@gmail.com).

R.-J. Shiue and D. Englund are with the Department of Electrical and Computer Science, Massachusetts Institute of Technology, MA 02139 USA (e-mail: tedshiue@mit.edu; englund@mit.edu).

Y. Gao and J. Hone are with the Department of Mechanical Engineering, Columbia University, NY 10027 USA (e-mail: yg2221@columbia.edu; jh2228@columbia.edu).

S. Assefa is with the IBM T. J. Watson Research Center, Yorktown Heights, NY 10598 USA (e-mail: sassefa@us.ibm.com).

Color versions of one or more of the figures in this paper are available online at http://ieeexplore.ieee.org.

Digital Object Identifier 10.1109/JSTQE.2013.2273412

accurately described in the framework of coupled mode theory, which will be detailed below (see Section II-A). Based on this model, we will then describe three optical effects resulting from the enhanced light–matter interaction: cavity-enhanced optical absorption (see Section II-B), enhanced Raman scattering (see Section II-C), and the enhancement of hot carrier spontaneous emission (SE) via the cavity Purcell effect (see Section II-D). In the configuration of a bus waveguide-integrated graphene, the long interaction length allows efficient absorption across a broad spectrum (without resonant enhancement). In Section III, we describe an experiment in which graphene is coupled to a silicon waveguide, resulting in a 6.2-dB attenuation over a length of 70 μm. The cavity-coupled graphene geometry promises high-performance graphene optoelectronic devices. In Section IV-A, we then modulate the cavity reflection by electrical tunings of graphene's Fermi energy. The cavity Finesse multiplies the otherwise weak absorption of graphene to a strong effect and enables a modulation contrast as high as 10 dB. Furthermore, we fabricate a cavity-graphene modulator with a response bandwidth as high as 0.57 GHz (see Section IV-B).

II. Coupled Graphene-Nanocavity System

We first theoretically modeled the coupled graphene-cavity system with a coupled-mode theory [16], and then experimentally measured the enhanced light–matter interaction on different integrated graphene–PPC nanocavity devices. In these studies, the PPC nanocavities were fabricated in membranes of silicon (Si, for near-infrared spectrum) or gallium phosphide (GaP, for visible spectrum) using a combination of electron beam lithography and dry/wet etching steps [17]. Devices were assembled using single-layer graphene prepared by mechanical exfoliation or chemical vapor deposition (CVD), which were then transferred onto the PPC nanocavities [18].

A. Coupled Graphene-Cavity Model

Fig. 1(a) shows the schematic of the coupled graphene-cavity model. The cavity mode $\mathbf{c}$ couples with the graphene and a propagating mode, which is sketched here in the form of a waveguide. The waveguide has forward and backward propagating modes, Mode $\mathbf{a}$ and Mode $\mathbf{b}$, which couple with the cavity resonance at rates of κ_{ca} and κ_{cb}, respectively. The incoming (outgoing) light of Mode $\mathbf{a}$ and Mode $\mathbf{b}$ are denoted by $\mathbf{a_{in}}$ ($\mathbf{a_{out}}$) and $\mathbf{b_{in}}$ ($\mathbf{b_{out}}$), respectively. We assumed the unloaded cavity (without the integration of graphene) has an intrinsic resonant frequency ω_0 and an energy decay rate $\kappa_{c'}$ due to radiative and absorptive losses. The Q factor of the waveguide-coupled cavity is determined by the total intrinsic loss $\kappa_c = \kappa_{c'} + \kappa_{ca} + \kappa_{cb}$ with $Q = \omega_0/\kappa_c$. When perturbed by a graphene sheet, the cavity mode undergoes a resonant frequency shift of $\Delta\omega$ and an increase in energy loss rate κ_{cg} due to the graphene absorption.

In the weak cavity-waveguide coupling regime, the graphene-cavity system can be described by the temporal coupled-mode equations [19]. By solving these equations and assuming only Mode $\mathbf{a}$ to be excited, we obtained the system reflection $R(\omega)$

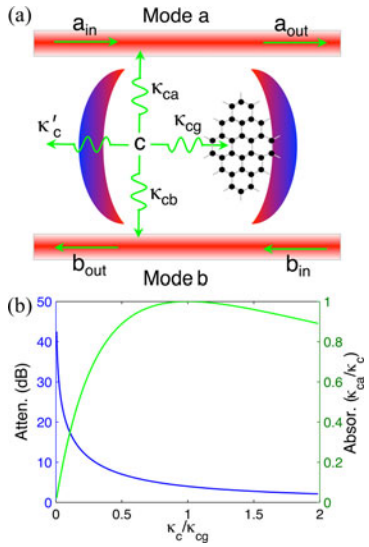

Fig. 1. (a) Schematic of the coupled graphene-cavity model. The cavity integrated with graphene is forward and backward coupled with Mode $\mathbf{a}$ and Mode $\mathbf{b}$, respectively. κ_c is the total energy decay rate of the intrinsic cavity, which consists of the coupling rates κ_{ca} and κ_{cb} into the waveguide modes, and decay rate $\kappa_{c'}$ caused by other lossy modes and material absorption. The graphene absorption induces the decay rate κ_{cg}. (b) Calculated relative attenuation of the cavity reflectivity (left scale) and the graphene absorbance (right scale) for the graphene-cavity system versus the ratio of the cavity decay rates κ_c/κ_{cg}.

and transmission $T(\omega)$ coefficients [16]

$$R(\omega) = \left|\frac{\mathbf{b_{out}}}{\mathbf{a_{in}}}\right|^2 = \frac{\kappa_{ca}\kappa_{cb}}{(\omega_0+\Delta\omega-\omega)^2+(\kappa_c/2+\kappa_{cg}/2)^2} \quad (1)$$

$$T(\omega) = \left|\frac{\mathbf{a_{out}}}{\mathbf{a_{in}}}\right|^2 = \frac{(\omega_0+\Delta\omega-\omega)^2+(\kappa_{cg}/2+\kappa'_c/2+\kappa_{cb}/2-\kappa_{ca}/2)^2}{(\omega_0+\Delta\omega-\omega)^2+(\kappa_c/2+\kappa_{cg}/2)^2}. \quad (2)$$

The loss of the system $(1-T-R)$ arises from the intrinsic cavity loss and the graphene absorption. The graphene absorption $A(\omega)$ is given by

$$A(\omega) = \frac{\kappa_{ca}\kappa_{cg}}{(\omega_0+\Delta\omega-\omega)^2+(\kappa_c/2+\kappa_{cg}/2)^2}. \quad (3)$$

For a given system, this absorption spectrum peaks at the resonant frequency of the graphene-cavity. In absence of the graphene layer, the same expressions apply on the cavity signal with $\kappa_{cg} = 0$ and $\Delta\omega = 0$.

From above expressions of the cavity reflection R and graphene absorption A, we can easily deduce the effect of the interaction between graphene and the localized cavity mode with respect to the ratio κ_c/κ_{cg}, as shown in Fig. 1(b). The blue curve shows the reflectivity attenuation of the cavity at the frequency of ω_0, defined as $10\log_{10}(R_{\text{intrinsic}}(\omega_0)/R_{\text{graphene}}(\omega_0))$, versus κ_c/κ_{cg}. The attenuation ratio for the reflectivities with and without graphene as $(1+\kappa_{cg}/\kappa_c)^2$ indicates that the reflectivity of the graphene-cavity system can be dramatically modulated by altering the parameter κ_c/κ_{cg}. For a high-Q cavity

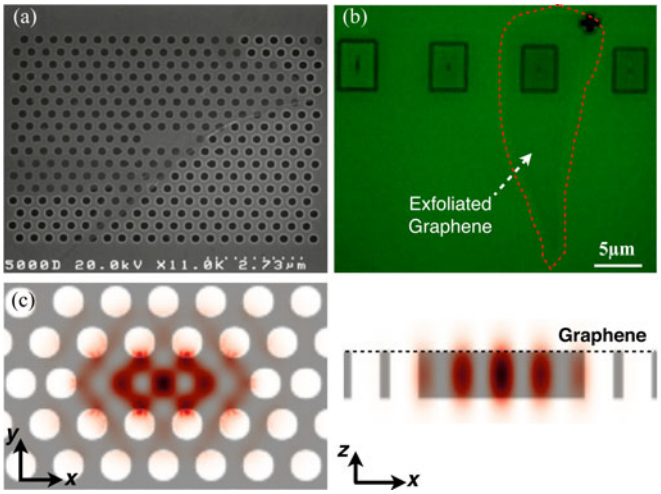

Fig. 2. (a) SEM image of a PPC cavity integrated with single-layer graphene. The folded edge shows the location of the graphene layer. (b) Optical microscope images of a PPC cavity integrated with single-layer graphene, which is marked with the red dashed line. (c) Simulated energy distribution of fundamental resonant mode of the L3 cavity using 3-D FDTD method, shown in plane (left) and in cross section (right). The graphene layer interacts with the evanescent field.

($Q \sim 2,600$), even the small absorption due to a monolayer of graphene can result in a transmission loss as high as 20 dB [16]. The graphene absorbance at the frequency of $\omega_0 + \Delta\omega$ versus κ_c/κ_{cg} is shown in the green curve of Fig. 1(b). Unlike the modulation of the cavity reflectivity, the on-resonance absorbance of graphene has a maximum value of κ_{ca}/κ_c, which is reached by optimizing the system decay rates to satisfy $\kappa_{cg} = \kappa_c$. This critical coupling condition indicates that matching the graphene-induced loss to the intrinsic cavity loss yields maximal absorbance in graphene. In general, the cavity resonance has the same forward and backward coupling rate, i.e., $\kappa_{ca} = \kappa_{cb}$. The maximum absorbance in graphene can reach 50% if the waveguide-cavity coupling is responsible for the entire intrinsic loss of the cavity, i.e., $\kappa_{ca} + \kappa_{cb} = \kappa_c$. However, in cavities having the traveling-wave resonant mode, such as ring-resonators [20], there is no backward coupling, which enables maximum absorbance of 100% in graphene.

B. Cavity-Enhanced Absorption in Graphene

Fig. 2(a) and (b) shows scanning electron microscope (SEM) and optical microscope images of the completed devices with exfoliated monolayer graphene sheets. The PPC cavities were fabricated on a silicon-on-insulator (SOI) wafer with the top Si membrane thickness of 220 nm. The PPC lattice has a lattice spacing $a = 450$ nm and a radius of air-holes $r = 0.29a$. The cavity is a linear three-hole defect cavity (L3) [21]. Micro-Raman spectroscopy was used to verify the presence of a single atomic layer of graphene on the PPC cavity.

From the simulated energy distribution of the fundamental resonant mode shown in Fig. 2(c), we see the coupling between the graphene layer and the evanescent field of the cavity mode. The coupling strength can be obtained from the resonant

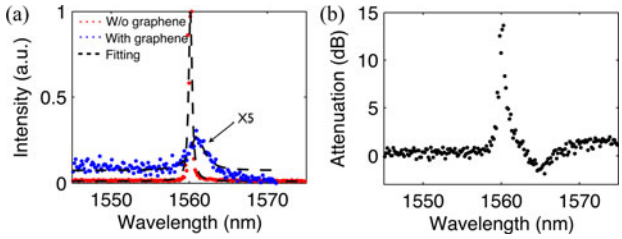

Fig. 3. Characterization of a PPC cavity coupled with a graphene monolayer. (a) Reflection spectra of the PPC cavity before and after (magnified five times) the deposition of an exfoliated graphene monolayer. (b) Spectrum of the relative attenuation of the cavity reflections with and without graphene. At the resonant wavelength of the unloaded cavity, the attenuation increases by 14 dB by inserting a single layer of graphene.

frequency shift $\Delta\omega$ and energy loss κ_{cg} [19]

$$\Delta\omega = -\frac{\omega_0}{2}\frac{\int \mathrm{d}^3\mathbf{r}((\varepsilon_{g1\parallel}(\mathbf{r})-1)|\mathbf{E}_{\parallel}(\mathbf{r})|^2+(\varepsilon_{g1\perp}(\mathbf{r})-1)|\mathbf{E}_{\perp}(\mathbf{r})|^2)}{\int \mathrm{d}^3\mathbf{r}\varepsilon_s(\mathbf{r})|\mathbf{E}(\mathbf{r})|^2} \tag{4}$$

$$\kappa_{cg} = \omega_0 \frac{\int \mathrm{d}^3\mathbf{r}\varepsilon_{g2\parallel}(\mathbf{r})|\mathbf{E}_{\parallel}(\mathbf{r})|^2}{\int \mathrm{d}^3\mathbf{r}\varepsilon_s(\mathbf{r})|\mathbf{E}(\mathbf{r})|^2}. \tag{5}$$

Here, the graphene layer is assumed to have an anisotropic complex dielectric function with in-plane and vertical components given by $(\varepsilon_{g1\parallel} + \mathbf{i}\varepsilon_{g2\parallel})$ and $(\varepsilon_{g1\perp} + \mathbf{i}\varepsilon_{g2\perp})$. The complex resonant field $\mathbf{E}(\mathbf{r})$ has in-plane and vertical components of $\mathbf{E}_{\parallel}(\mathbf{r})$ and $\mathbf{E}_{\perp}(\mathbf{r})$. By controlling the sub-wavelength-scale slab thickness between $d = 0.29a$–$0.65a$, it is possible to control the strength of the evanescent field amplitude on graphene E_{graphene} between 0.1 and 0.4 of the maximum amplitude ($E_{\max}$). This, in turn, enables control of the coupling rate between the graphene sheet and the cavity field.

The completed devices were characterized using a cross-polarization confocal microscope with a broad-band illumination input light source [22]. Fig. 3(a) shows reflection spectra $R(\omega)$ of the PPC cavity displayed in Fig. 2(b) before and after the graphene deposition. The graphene layer lowered the Q factor to 700 from an original value of 3200 and red-shifted the resonance by 0.9 nm from 1560.1 nm. The strong attenuation of the cavity reflection is summarized in Fig. 3(b). Through the enhanced light–matter interaction in the cavity, the weakly absorbing graphene rendered the cavity nearly opaque with an 14-dB attenuation.

The experimental observations can be explained using the above coupled graphene-cavity model. On the cross-polarization microscope, the propagating modes of the waveguide can be considered as the approximately Gaussian spatial modes corresponding to the excitation and collection channels of the microscope. The intrinsic loss of the unloaded cavity is attributed to out-of-plane radiation with an energy decay rate of $\kappa_c = \omega_0/Q$, where ω_0 is the resonant frequency. We assumed a coupling efficiency η between the Gaussian spatial mode and the cavity radiation field so that the cavity mode couples with the excitation and collection microscope modes at a rate $\eta\kappa_c$.

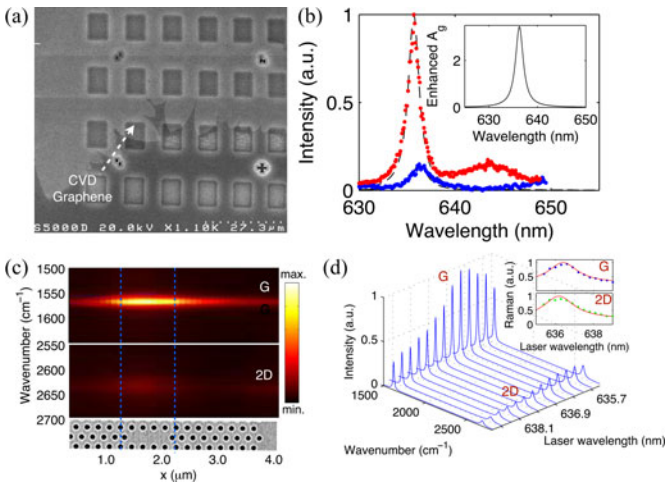

Fig. 4. Enhanced Raman scattering from a graphene-cavity device. (a) SEM image of PPC cavities integrated with a large CVD-grown graphene flake. (b) Reflection spectra of the cavity before and after the deposition of graphene, inset: calculated absorbance enhancement of the device. (c) Spatial dependence of the cavity-enhanced Raman scattering process, displaying strong scattering when illuminated near the cavity defect region (indicated by the bottom SEM image). (d) Laser wavelength dependence of the Raman scattering. (Adapted with permission from [16]. Copyright (2012) American Chemical Society.)

The experimental reflection spectra shown in Fig. 3(a) can be accurately fitted by (1) and (3) for $\kappa_c = 1.6 \times 10^{-4}\omega_0, \Delta\omega = -0.58 \times 10^{-3}\omega_0$, and $\kappa_{cg} = 1.11 \times 10^{-3}\omega_0$. Thus, for the device considered here, $\Delta\omega$ and κ_{cg} are comparable in magnitude and far exceed κ_c. This indicates that the graphene layer dominates the photon loss in the cavity with a fraction of $\kappa_{cg}/(\kappa_{cg} + \kappa_c) \approx 87\%$.

C. Cavity-Enhanced Raman Scattering

We have recently shown that the enhanced light–matter interaction in the cavity can greatly enhance the Raman scattering efficiency of graphene [16]. The results are summarized here. Since the Raman scattering rate from graphene layer is proportional to the excitation field at the graphene location, we should expect a stronger Raman signal when the graphene is close to the field maximum of the cavity mode. For these measurements, we employed L3 PPC cavities in a 138-nm-thick GaP membrane with a lattice spacing of $a = 170$ nm and an air-hole radius of $r = 79$ nm. The cavity modes are resonant in the visible spectral range. This device was coupled to a CVD-grown graphene layer, as shown in the SEM image of Fig. 4(a). Fig. 4(b) shows the reflection measurements of the cavity. The Q factor of the cavity dropped from 860 to 330 and the resonance is red-shifted from 635.7 to 636.3 nm when graphene is coupled to the cavity. When excited by a laser at 637 nm, the graphene layer showed clear peaks at Raman shifts of 1578 and 2640 cm^{-1}, corresponding to the well-known G and 2-D bands, respectively. A spatial scan across the PPC cavity along the x-axis [shown in Fig. 4(c)] shows that the Raman scattering is enhanced dramatically when pumped through the nanocavity defect. We verified the effect of the cavity-enhanced pump by sweeping the laser wavelength from 635 to 639 nm, covering the graphene-cavity resonance, as shown in Fig. 4(d). The pump-wavelength dependences of the G and 2-D bands, plotted in the inset of Fig. 4(d), both followed the expected Lorentzian lineshape function centered at 636.3 nm with a Q factor of 330, consistent with the cavity resonance. In these measurements, the flat baseline arises from incident radiation that excites the graphene directly, not through the cavity mode. Normalizing the peak Raman signals to the baseline, we obtained a 2.8- and a 3.3-fold increase of the G and 2-D bands, respectively.

This wavelength dependence of the Raman scattering matches the expected cavity-field enhancement. The cavity reflection spectra in Fig. 4(b) indicate a cavity resonance shift of $\Delta\omega = -0.9 \times 10^{-3}\omega_0$, and an energy decay of $\kappa_{cg} = 1.9 \times 10^{-3}\omega_0$. By estimating a coupling efficiency of $\eta \approx 4\%$ from simulations of the cavity field and the numerical aperture (NA $= 0.95$) of the objective lens used in this experiment [23], we calculated the absorbance of this device to be 1.88% on resonance. For the graphene layer on the bulk GaP membrane, the absorbance is about 0.54% as estimated from Snell's law [16]. The inset of Fig. 4(b) plots the spectrally resolved cavity-enhanced graphene absorbance. This shows a maximum on-resonance enhancement factor of 3.4, which is close to the enhancement of the graphene Raman scattering.

D. Cavity-Enhanced Photoluminescence

It is well known that the high Q factor and small mode volume of PPC nanocavities can lead to a large enhancement of the SE rate of radiative dipoles coupled to the cavity both spectrally and spatially. This Purcell enhancement can be exploited to enhance the photoluminescence (PL) from hot carriers in graphene through the increased electromagnetic density of states. We excited another cavity-graphene device shown in Fig. 4(a) with a pulsed Ti:Sapphire oscillator, which produced 150-fs laser pulses centered at a wavelength of 800 nm and with a repetition rate of 76 MHz. The green curve in Fig. 5(a) shows the hot PL emission from graphene. The pump is not on resonance with any cavity modes and the polarization of the PL is filtered perpendicularly to the far-field radiation of the cavity mode ($\phi = 90°$) such that it largely represents a pure emission from graphene not modified by the presence of the cavity. Such a broadband emission (only observable with femtosecond pumping) with photon energies higher than the pump energy has been attributed to thermal emissions from a largely thermalized electronic subsystem, with elevated temperatures existing on the femtosecond to picosecond time scale [24]. The emission spectrum covered two of the resonance modes of our cavity, which is shown in the inset of Fig. 5(b). The particular graphene-cavity structure had resonant modes centered at wavelengths of 636.3 nm (mode 1) and 642.9 nm (mode 2) with Q factors of 250 and 480, respectively. From 3-D finite-difference time-domain (FDTD) simulations, we estimated that these modes had volumes of $V_{\text{mode},1} = 0.36(\lambda/n)^3$ and $V_{\text{mode},2} = 0.68(\lambda/n)^3$, with corresponding mode energy distributions shown in Fig. 5(c). In contrast, when we changed the polarizer to collect radiation along the radiative axis of the cavity modes ($\phi = 0°$) [red curve in Fig. 5(a)], enhanced emission centered at the corresponding cavity resonances is clearly visible, while the rest of emission

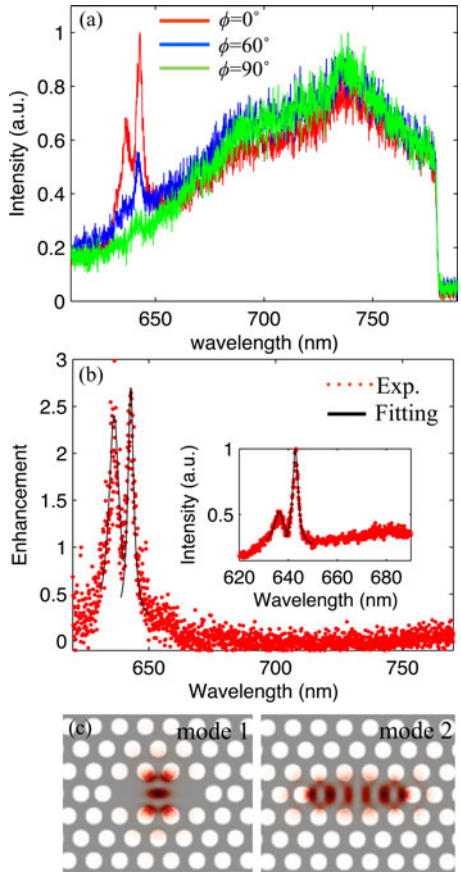

Fig. 5. Purcell-modified SE from the graphene by the nanocavity. (a) PL spectra of graphene under different polarizations. The angle ϕ is defined as the angle between the polarization of the polarizer and the direction of the cavity far-field emission. (b) Cavity-enhancement spectrum of the PL emission, inset: reflection spectrum of the cavity, showing the agreement of the PL enhancement peaks and the cavity modes. (c) Energy field distributions of the simulated cavity modes, left: mode 1, right: mode 2.

spectrum is almost unaffected, consistent with the unpolarized character of thermal emission.

Comparing the PL spectra measured with $\phi = 90^\circ$ and 0°, we obtained the spectrally resolved cavity-enhanced collected emission, as shown in Fig. 5(b), with two enhancement features peak at $\sim$2.5 coinciding with the cavity resonances. This spectrally selective enhancement is attributed to the Purcell enhancement of the SE rate and the enhancement of light collection from the cavity mode compared to the collected emission from the graphene on bulk GaP membrane. Quantitatively, the SE rate modification by the cavity can be analyzed by considering the graphene layer as a collection of dipole emitters. Let us consider a particular dipole μ at a position $\mathbf{r}$ in the graphene layer located on the bulk membrane. We assumed it has a natural SE rate of $\Gamma_0(\lambda)d\lambda$ with transitions corresponding to the spectral range from λ to $\lambda + d\lambda$. Since the SE efficiency is very low, the emission rate scales with the Purcell effect. The modified SE distribution when the graphene sheet is on the PPC nanocavity is given by

$$\Gamma(\lambda) = \Gamma_0(\lambda) F_{c,0} L(\lambda) |\psi|^2. \quad (6)$$

Here, $L(\lambda)$ denotes the cavity's Lorentzian spectrum, $F_{c,0} = \frac{3}{4\pi^2}\frac{Q}{V_{\mathrm{mode}}}(\frac{\lambda_{c,0}}{n})^3$ is the maximum SE enhancement (Purcell) factor of the cavity mode, and $\psi = \mathbf{E}\cdot\mu/\mathbf{E}_{\max}\cdot\mu$ denotes the mode overlap between the emitter electric dipole moment μ and the cavity field $\mathbf{E}$.

The total emission spectrum $I_\phi(\lambda)$ from the cavity collected with different polarization angles ϕ can be calculated by integrating the SE rate given in (6) over the spatial, spectral, and orientation density of the emitter dipoles $\rho(\mathbf{r}, \lambda, \mu)$

$$I_\phi(\lambda) = \Gamma_0(\lambda)\int \mathrm{d}\mu\mathrm{d}\lambda\mathrm{d}^3\mathbf{r}\rho(\mathbf{r},\lambda,\mu)\{\eta_{\mathrm{c},0}F_{\mathrm{c},0}L(\lambda)|\psi|^2\sin(\phi) + \Gamma_0(\lambda)\int \mathrm{d}\mu\mathrm{d}\lambda\mathrm{d}^3\mathbf{r}\rho(\mathbf{r},\lambda,\mu)\eta_{\mathrm{bulk}}\}. \quad (7)$$

Here, the second term denotes the collected emission from the emitters uncoupled with the cavity mode. $\eta_{\mathrm{c},0}$ and η_{bulk} are the collection efficiencies into the objective lens of the emission from the cavity mode and the bulk membrane, respectively. By numerically integrating the cavity emission profile over the numerical aperture (NA $= 0.95$) of the objective lens, we obtained ratios of $\eta_{\mathrm{c},0}/\eta_{\mathrm{bulk}} \approx 2.3$ and 1.8 for modes 1 and 2, respectively [23], [25].

The spectrally resolved enhancement of the PL emission from the graphene shown in Fig. 5(b) is

$$\frac{I_{0^\circ}(\lambda)}{I_{90^\circ}(\lambda)} - 1 = \frac{\eta_{c,0}}{\eta_{\mathrm{bulk}}}F_{\mathrm{c},0}\iiint \mathrm{d}\mu\mathrm{d}\lambda\mathrm{d}^3\mathbf{r}L(\lambda)|\psi|^2. \quad (8)$$

The factors $L(\lambda)$ of the two resonant modes fit the profiles of the two enhanced peaks shown in Fig. 5(b) well. The integral over the angle of the dipole μ with respect to the cavity field $\mathbf{E}$ equals to 1/2 due to the random orientations of dipoles on the 2-D graphene sheet. The spatial density of the dipoles corresponds to the excitation and collection from a uniform graphene sheet excited by a Gaussian beam with a full-width at half-maximum of about 400 nm in the xy plane. Over this excitation area, the spatial integrals of $(|\mathbf{E}\|\mu|/|\mathbf{E}_{\max}\|\mu|)^2$ are 0.045 and 0.067 for cavity modes 1 and 2 calculated from the mode profiles shown in Fig. 5(c). With the experimentally obtained Q factors, we obtained $F_{c,0}$ as 52.8 for mode 1 and 53.7 for mode 2. Solving (8) with the above estimations, we obtained the maximum on-resonance enhancement factors for the spatially averaged emission spectrum for the two modes as 2.73 and 3.23, respectively. These model calculations fit nicely to the experimental results shown in Fig. 5(b), with peak enhancement of 2.37 and 2.52 for modes 1 and 2, respectively.

III. Enhanced Absorption in Waveguide-Integrated Graphene

So far, we have described the enhancement of the light–matter interaction via optical resonators. This effect is inherently narrow-band. Coupling graphene with a single-mode bus waveguide can enhance the light–graphene interaction across a broad spectrum due to the large extension of the interaction length. Fig. 6(a) shows an optical microscope image of a fabricated graphene-waveguide device, with a $\sim$70-μm-long mechanically exfoliated graphene bilayer transferred onto a bus

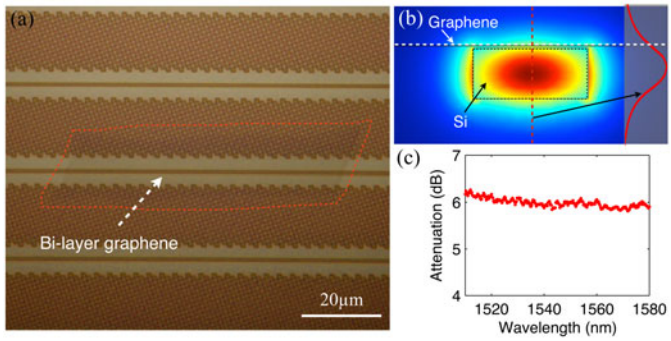

Fig. 6. Waveguide-integrated graphene for enhanced absorption. (a) Optical microscope image of the waveguide-integrated graphene bilayer. (b) Simulated guided TE mode of the waveguide with a graphene bilayer on top. The right red curve shows the mode profile in the middle of the structure. (c) Spectrally resolved transmission loss of the waveguide.

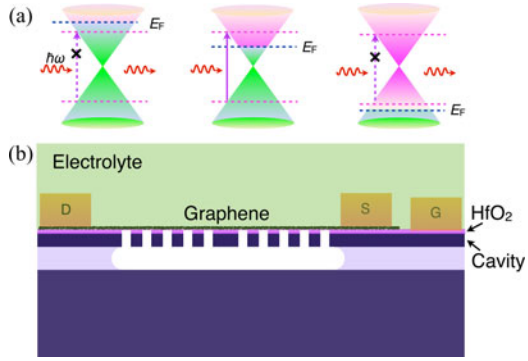

Fig. 7. (a) The band structures of graphene at different doping levels; graphene becomes more transparent when interband transitions are Pauli blocked, as shown in images on the left and right. (b) Schematic of the electrically controlled graphene-PPC nanocavity. A thin hafnium oxide (HfO_2) layer is grown on the chip before the graphene transfer to isolate the Si slab and graphene electrically. The cavity reflection can be modulated by tuning the Fermi level of graphene with the doping from the top electrolyte layer.

waveguide. The silicon waveguides were fabricated from an SOI wafer with a 220-nm-thick Si membrane using the standard shallow trench isolation (STI) module. A waveguide width of 520 nm was chosen to ensure a single transverse electrical (TE) mode with low transmission loss. To prevent the graphene from fracturing at the edges of the waveguide, the chip was planarized by back-filling with a thick SiO_2 layer and then a chemical mechanical polishing to reach the top Si layer. A $\sim$10-nm-thick SiO_2 layer was deposited on the chip to ensure electrical isolation of the graphene layer from the Si membrane in future devices. The bilayer graphene was deposited on the waveguide using a precise alignment technique. To analyze the strong interaction between the graphene and light transmitting in the waveguide, we simulated the guided mode of the device using a finite element method (COMSOL). The thickness of the bilayer graphene was taken to be 1.4 nm and the refractive indices of SiO_2, Si, and graphene were 1.48, 3.4, and $2.38 + 1.68i$ for the light at the wavelength of 1550 nm [26], respectively. Fig. 6(b) displays the simulated TE field distribution of the guided mode, showing the evanescent field of the waveguide mode, which couples with the graphene layer. The field profile along the middle of the waveguide shows that the electrical field located on the graphene layer is about 40% of the maximum electrical field. From the complex effective index of the simulated guided mode, we estimated the absorption coefficient of the graphene bilayer to be 0.085 dB/μm.

The integrated graphene-waveguide system was characterized by coupling light from lensed fibers into and out of the waveguide via SU8 edge-couplers at opposite ends of the Si waveguide. The polarization of the input was controlled using a fiber-based polarizer to match the TE mode of the waveguide. A tunable continuous-wave (CW) laser was used as the excitation source. The characterization result is shown in Fig. 6(c). From the measurements of waveguide transmissions before and after the graphene transfer, we estimated that the 70-μm-long graphene bilayer causes a uniform transmission loss around 6.2 dB over the wavelength range from 1510 to 1580 nm—much greater than the 0.1 dB absorption in the normal-incidence configuration. The transmission loss indicates an absorption coefficient of 0.089 dB/μm at the wavelength of 1550 nm, which is larger than that obtained in the mode simulation. We attributed the greater absorption coefficient to the extra loss caused by the scattering and back-reflection at the graphene/waveguide interface. By coupling graphene with a transverse magnetic guided mode of the waveguide [4] or with waveguides having thinner thickness [27], the graphene absorption coefficient can be improved to about 0.2 dB/μm.

IV. Electrooptic Modulation of a Photonic Crystal Nanocavity by Electrical Gating of Graphene

Due to the high Fermi velocity the Dirac electrons are traveling at, the optical transmission of monolayer graphene for incident light at frequency ω can be widely modulated by electrostatically tuning the graphene's Fermi energy (E_F). As indicated in Fig. 7(a), when E_F is tuned away from the Dirac point by more than half of the photon energy $\hbar\omega/2$, the interband transitions become forbidden by Pauli blocking, reducing the graphene absorption [28], [29]. Because of the cavity-enhanced absorption into the graphene layer, the cavity reflection is very low when the Fermi energy is near the Dirac point. By tuning the Fermi energy to reduce the absorption, the reflection of the cavity can thus be increased to achieve a high modulation depth.

A. High-Contrast Electrical Modulation of the Graphene-Cavity Reflection

We recently demonstrated such a cavity-enhanced modulation based on a graphene sheet coupled to a silicon PPC air-slot cavity (see Fig. 8), which increased graphene-field overlap compared to the L3 cavity and enabled a modulation depth in excess of 10 dB [13]; a similar experiment reached a modulation depth up to 6 dB in an L3 PPC cavity [14]. The experimental device consists of a graphene field-effect transistor (FET) coupled to a nanocavity, schematically shown in Fig. 7(b). The graphene FET is gated with a solid electrolyte (PEO plus $LiClO_4$) to reach high electrical fields and carrier densities in graphene [29]–[31]. Applying a gate voltage (V_g) between gate and drain electrodes controls the doping level of the graphene layer.

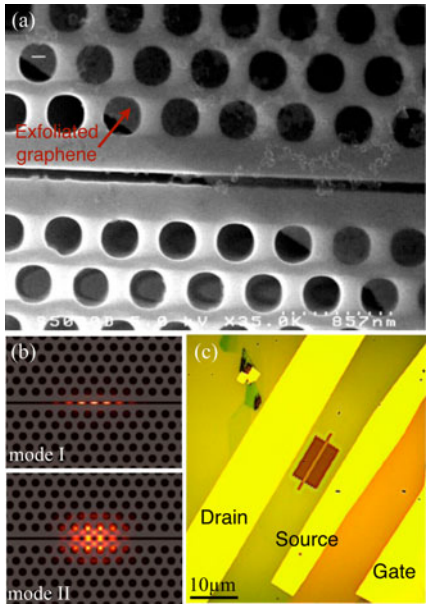

Fig. 8. (a) SEM image of an air-slot cavity integrated with a graphene flake. (b) Simulated energy distributions of two resonant modes of the air-slot cavity. (c) Optical microscope image of one of the electrically controlled graphene-PPC nanocavity devices. (Adapted with permission from [13]. Copyright (2013) American Chemical Society.)

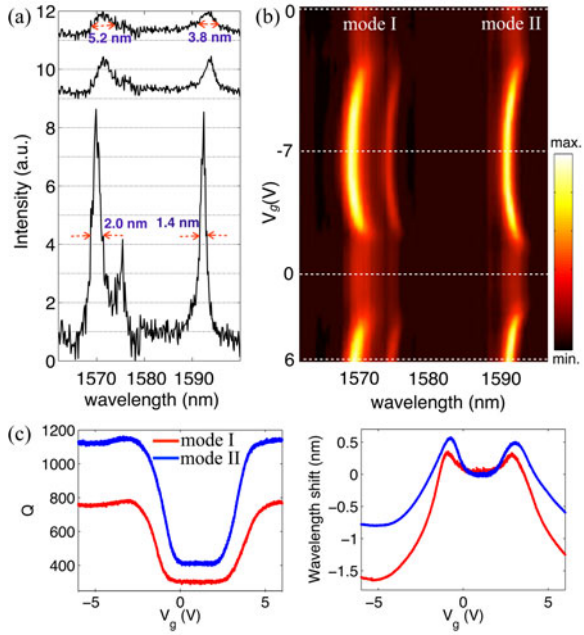

Fig. 9. Characterization of the electrically controlled graphene-PPC nanocavity. (a) Spectra of the cavity reflection for $V_g = 0$, -1, and -7 V (from top to bottom), which are normalized by the reflection peak at $V_g = 0$. (b) Reflection spectra of the cavity as V_g is modulated. The resonance peaks show clear wavelength shifts, modulations of Q factors and intensities under different gate voltages. (c) Measured variations of the Q factors and wavelength shifts for modes I and II as a function of V_g. (Adapted with permission from [13]. Copyright (2013) American Chemical Society.)

The air-slot PPC nanocavities were fabricated on the SOI wafer. The photonic crystal has a lattice spacing of $a = 450$ nm and an air-hole radius of $r = 150$ nm. The cavity had a defect formed by shifting air-holes away from the central slot [32]. Fig. 8(a) displays an SEM image of the slot cavity with a graphene flake. The two lowest energy simulated resonant modes of the slot cavity are shown in Fig. 8(b), which indicate that most of the light is confined in the air-gap. Compared to the L3 cavity, where light is confined in the high index material, the coupling rate of the slot cavity to the graphene sheet is approximately three times larger. After atomic layer deposition of HfO_2 and transfer of a mechanically exfoliated graphene monolayer, the drain, source, and gate electrodes of the graphene FET were fabricated using electron-beam lithography and titanium/gold (Ti/Au, 1 nm/40 nm) electron-beam evaporation. Finally, the electrolyte was spin-coated on the entire wafer. Fig. 8(c) shows a finished device in which the gate electrode is located about 15 μm from the graphene flake.

The cavity reflection was measured as a function of the gated voltage (V_g) using the cross-polarization confocal microscope. Simultaneously, the electrical resistance through source and drain electrodes was monitored to record the doping level of graphene. Fig. 9(a) displays the measured reflection spectra obtained with different gate voltages. The top spectrum displays the reflection from the cavity covering with the graphene and electrolyte, but with zero gate voltage ($V_g = 0$). Two resonant peaks are visible at wavelengths of 1571.7 nm (mode I) and 1593 nm (mode II) with Q factors of 335 and 410—these are expectedly low due to the strong coupling to the graphene sheet. Applying the gate voltage along the negative direction to -1 V, we observed the resonant peaks on the cavity reflection become narrower and higher, accompanied by a red-shift of the central wavelength, as shown in the second panel of Fig. 9(a). The further increased cavity reflection and Q factor were obtained with higher gate voltage, as shown in the third spectrum of Fig. 9(a) with $V_g = -7$ V. The intensities of the resonance peaks increase by a factor of 8.5 and the Q factors increase to 740 and 1150 for modes I and II, respectively. The two peaks also show obvious blue-shift of the resonance wavelengths. As the cavity peaks become narrower, another resonant mode at the wavelength of 1574.9 nm become distinguishable, which overlaps with the mode I due to the large graphene absorption at $V_g = 0$. The increased reflections and Q factors of the cavity indicate the electrical suppression of the graphene absorption due to the Pauli blocking. However, because of the phonon-assisted processes and charge inhomogeneity in the graphene layer [29], [31], the Pauli blocking is not complete even under high gate voltage. The remaining absorption results in the observation that the recovered Q factors of modes I and II are lower than those before the graphene transfer [13].

To test the modulation of the graphene-PPC cavity, we swept the gate voltage linearly in a saw-tooth pattern between -7 V and 6 V and acquired the spectra continuously at 30 frames per second, as shown in Fig. 9(b). In terms of the overall response to gating, we observed the symmetric modulation of the cavity with negative (hole-doped) and positive (electron-doped) gate voltages with respect to the charge neutrality point of the graphene layer located at $V_{CN} = 1$ V. The neutrality point was also confirmed from the maximum electrical resistance peak of graphene. We observed the abrupt changes of the reflection

intensity of modes I and II take place when V_g changed in -1 to -2.5 V and 3 to 4.5 V, which indicates the Fermi energy shift of graphene past $E_F = \hbar\omega/2$ for the onset of Pauli blocking. Under other high or low gate voltages, the intensities of the cavity peaks have no observable variations. The corresponding modulations on the Q factor for modes I and II are shown in Fig. 9(c). The variation trends of Q factors are similar to that of the mode intensities, consistent with the conclusion from the attenuation curve shown in Fig. 1(b). Fig. 9(d) displays the wavelength-shifts of the resonant modes with electrical gating, showing large blue-shifts of both modes (total excursions of 2 and 1.3 nm for modes I and II) after slight red-shifts under low doping-level. The observed variations of the Q factors and wavelengths of the resonances arise from the modifications in the complex in-plane optical sheet conductivity of graphene; this observation can be explained well by a theoretical model [13]. Considering the intensity magnification and wavelength-shift of the resonant modes, the modulation depth at the peak wavelength for the highly doped graphene is high. For example, at the wavelength of 1592.9 nm, we obtained a modulation depth exceeding 10 dB for a swing gate voltage between -1 and -2.5 V.

B. High-Speed Graphene-Cavity Modulator

While the speed of the above device is limited by the ionic mobility of the solid electrolyte [33], the use of highly doped silicon PPC cavity as a back gate or the inclusion of dual-gated graphene layers should permit an increase of the modulation speed into the gigahertz regime in view of the ultrafast carrier dynamics for both electrons and holes in graphene [4], [11], [34]. Already, a broad-band modulator was demonstrated at a frequency near 1 GHz with a 6-dB modulation contrast [11]. Here, we described a cavity-based modulator employing a graphene capacitor consisting of two graphene monolayers separated by a boron nitride (BN) dielectric layer. This dual-gated graphene capacitor geometry provides the contact and modulation contrast when coupled to the cavity. Alternatively, a doping layer in the silicon cavity could replace one of the graphene layers as an electrical contact, though the doping layer may cause additional cavity loss compared to the "semitransparent" graphene contact. Fig. 10(a) displays the device schematically. The bottom graphene is electrically isolated from the substrate membrane with a thin dielectric layer. Two graphene layers are separated by another dielectric layer to construct a parallel-capacitor. When a bias voltage V_g is applied across the two graphene layers, the two graphene plate conductors are doped with the similar Fermi level and reach optical transparency simultaneously. The reduction of the absorption of the dual graphene layers enables more efficient modulation of the cavity reflection.

A fabricated device shown in Fig. 10(b) consists of a Si L3 PPC cavity and a dual-layer graphene capacitor. A 10-nm HfO_2 layer was grown on the cavity using atomic layer deposition. Two graphene monolayers surrounding a 7.6-nm-thick BN spacer layer were transferred onto the cavity one-by-one, using a precision transfer technique [18]. Two Ti/Au electrodes were deposited separately on the top and the bottom graphene layers,

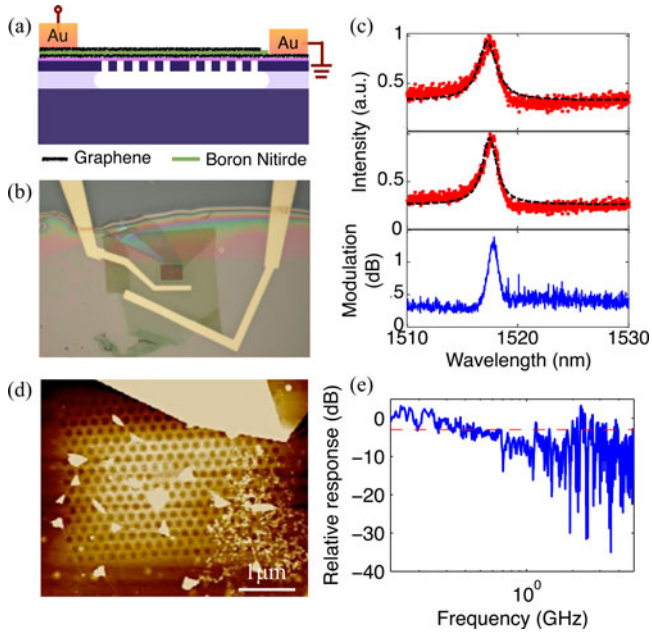

Fig. 10. Characterization of the high-speed cavity-graphene electro-optic modulator. (a) Schematic of the cavity-graphene modulator based on dual graphene layers. (b) Optical microscope image of a fabricated device. (c) Reflection spectra of the cavity with the gated voltage of 0 V (top), 2.5 V (middle), and the spectrally resolved modulation between the two reflection spectra (bottom). (d) Atomic force microscope image of the device. (e) Dynamics response of the modulator.

which are separated by the BN dielectric layer. Fig. 10(c) shows the reflection spectra obtained with bias voltages of 0 and 2.5 V, together with the spectrally resolved modulation between the two bias voltages. As was found for the electrolyte-modulated device described above, when a bias voltage was applied on the graphene–BN–graphene capacitor, the resonant cavity peak became narrower and higher while the wavelength shifted. Under 2.5-V bias voltage, the Q factor of the cavity increased from 770 to 960 and the resonant wavelength red-shifted from 1517.9 to 1518.1 nm. The modulation spectrum indicates a maximum modulation depth close to 1.5 dB at the resonant wavelength of 1518.1 nm. In the electrolyte-gated device, when the Fermi level of the graphene layer was tuned past $E_F = \hbar\omega/2$ to bring the device into the Pauli blocking regime, the resonant wavelength went through a red-shifting process was already strongly blue-shifted [see Fig. 9(b)]. On the other hand, in the graphene-BN-graphene dual-gated device, the spectra in Fig. 10(c) show that the doping of the graphene layers causes resonant wavelength just start to red-shift, which is far from the wavelength blue-shift and Pauli blocking regime. Based on the gating results shown in Fig. 9(b) and the wavelength red-shift of the current device, a modulation depth higher than 10 dB would be expected for higher bias voltage. However, the voltage was limited to $\sim$2.5 V by the current leaking of the capacitor, which was attributed to the unexpected defects during the multiple transfer processes, as shown in the atomic force microscope image of Fig. 10(d).

We characterized the frequency characteristics of the modulator by coupling a CW laser through the cavity at a wavelength

of 1518.1 nm. An ac electrical signal from a network analyzer was applied to the graphene capacitor via an RF microwave probe. A dc offset was added to the small ac signal to bias the applied voltage near the highest slope in the reflection modulation of the graphene-cavity modulator. The reflected cavity signal was detected via a high-speed InGaAs photodiode connected to the same network analyzer. The modulation response was then quantified through the $S21$ parameter in the frequency range from 20 MHz to 2 GHz, as shown in Fig. 10(e). The 3-dB cutoff frequency of the device is at about 0.57 GHz with static drive voltage of 2 V. We estimated that this response rate was limited primarily by the RC constant. The $S11$ parameter of the device indicated a capacitance C of about 1.1 pF. The capacitance is consistent with a calculation from the parallel-capacitance model, taking the dielectric constant of BN to be 3.9 and the area of the capacitor as 250 μm^2. The series resistance R measured from $S11$ is about 200 Ω, which is mainly caused by the contact resistance considering the low sheet resistance of the graphene layer. The calculated RC-limited bandwidth is, therefore, $1/(2\pi RC) = 0.72$ GHz. An estimation of the energy consumption E per bit switching of the current device can be derived by considering the energy required to charge (discharge) the graphene capacitor, which yields $E = CV_g^2/2$ [35]. Assuming a swing voltage of $V_g = 2.5$ V, and $C = 1.1$ pF, we estimated the energy consumption is about 3 pJ/bit, which is similar to the value reported for other electro-optic modulators with similar extinction ratio [36]. We expect that the dynamic response and energy consumption of the dual-gated graphene-PPC nanocavity modulator can be greatly improved by shaping the graphene parallel capacitor to cover only the defect region of the nanocavity, where the main resonant optical field locates, by a selective oxygen-plasma etching. In this case, the area of the graphene capacitor could be smaller than 1 μm^2, which would reduce the device capacitance by two orders of magnitude. Therefore, a dual-gated graphene-PPC nanocavity modulator could reach a response bandwidth greater than 100 GHz and energy consumption lower than 50 fJ/bit (note that the large spectral bandwidth of the graphene modulator would make it less sensitive to temperature changes than most ring-based modulators employing free carrier modulation). These figures make the graphene modulator promising for reaching energy targets in optical interconnects [35].

V. Conclusion

We have demonstrated that the interaction of light with graphene can be enhanced by coupling to a PPC nanocavity or a bus waveguide. We theoretically described the graphene-cavity system into a coupled-mode model, which indicates the controlling of graphene-cavity coupling by modifying the PPC slab thickness and intrinsic Q factors of the cavity. Due to the strong localization of the optical field in cavity, it is possible to dramatically enhance graphene absorption, Raman scattering, and PL emission through spectroscopic studies on the graphene-cavity coupled devices. The cavity-enhanced graphene absorption allows for the implementation of electro-optic modulation via the cavity reflection with high extinction ratio by electrically doping the graphene layer. Experimental results from a polymeric electrolyte gated graphene device showed a modulation depth higher than 10 dB. Using an integrated dual-gated graphene layer capacitor with a PPC cavity, we also demonstrated a graphene-cavity modulator operating at rates approaching 1 GHz. These studies show the promise of future graphene modulators that will combine high speed, high contrast, and low energy consumption. In contrast to the cavity enhancement effect, the bus waveguide controls the graphene–light interaction by different extensions of their coupling length over a broadband wavelength range. By measuring transmissions of a waveguide with and without graphene, we obtained a 6.2-dB transmission attenuation caused by the graphene absorption over a length of 70 μm in a wavelength range of 1510–1580 nm. The geometries of the graphene-PPC nanocavity and -waveguide, with the combined advantages of ease to fabrication, compact footprint, efficient light–matter interactions, promise a novel architecture for on-chip optical communications.

References

[1] R. R. Nair, P. Blake, A. N. Grigorenko, K. S. Novoselov, T. J. Booth, T. Stauber, N. M. R. Peres, and A. K. Geim, "Fine structure constant defines visual transparency of graphene," *Science*, vol. 320, no. 5881, p. 1308, 2008.

[2] T. Mueller, F. Xia, and P. Avouris, "Graphene photodetectors for high-speed optical communications," *Nature Photon.*, vol. 4, no. 5, pp. 297–301, Mar. 2010.

[3] F. Xia, T. Mueller, Y.-M. Lin, A. Valdes-Garcia, and P. Avouris, "Ultrafast graphene photodetector," *Nature Nanotechnol.*, vol. 4, no. 12, pp. 839–843, 2009.

[4] M. Liu, X. Yin, E. Ulin-Avila, B. Geng, T. Zentgraf, L. Ju, F. Wang, and X. Zhang, "A graphene-based broadband optical modulator," *Nature*, vol. 474, no. 7349, pp. 64–67, Jun. 2011.

[5] X.-L. Li, J.-L. Xu, Y.-Z. Wu, J.-L. He, and X.-P. Hao, "Large energy laser pulses with high repetition rate by graphene Q-switched solid-state laser," *Opt. Exp.*, vol. 19, no. 10, pp. 9950–9955, 2011.

[6] E. Hendry, P. Hale, J. Moger, A. Savchenko, and S. Mikhailov, "Coherent nonlinear optical response of graphene," *Phys. Rev. Lett.*, vol. 105, no. 9, pp. 97401–97404, 2010.

[7] J. Chen, M. Badioli, P. Alonso-González, S. Thongrattanasiri, F. Huth, J. Osmond, M. Spasenović, A. Centeno, A. Pesquera, P. Godignon, A. Z. Elorza, N. Camara, F. J. García de Abajo, R. Hillenbrand, and F. H. L. Koppens, "Optical nano-imaging of gate-tunable graphene plasmons," *Nature*, vol. 487, no. 7405, pp. 77–81, 2012.

[8] Z. Fei, A. S. Rodin, G. O. Andreev, W. Bao, A. S. McLeod, M. Wagner, L. M. Zhang, Z. Zhao, M. Thiemens, G. Dominguez, M. M. Fogler, A. H. Castro Neto, C. N. Lau, F. Keilmann, and D. N. Basov, "Gate-tuning of graphene plasmons revealed by infrared nano-imaging," *Nature*, vol. 487, no. 7405, pp. 82–85, 2012.

[9] M. Furchi, A. Urich, A. Pospischil, G. Lilley, K. Unterrainer, H. Detz, P. Klang, A. M. Andrews, W. Schrenk, G. Strasser, and T. Mueller, "Microcavity-integrated graphene photodetector," *Nano Lett.*, vol. 12, no. 6, pp. 2773–2777, Jun. 2012.

[10] M. Engel, M. Steiner, A. Lombardo, and A. C. Ferrari, "Light-matter interaction in a microcavity-controlled graphene transistor," *Nature Commun.*, vol. 3, p. 906, 2012.

[11] M. Liu, X. Yin, and X. Zhang, "Double-layer graphene optical modulator," *Nano Lett.*, vol. 12, no. 3, pp. 1482–1485, Mar. 2012.

[12] T. Gu, N. Petrone, J. F. McMillan, A. van der Zande, M. Yu, G. Q. Lo, D. L. Kwong, J. Hone, and C. W. Wong, "Regenerative oscillation and four-wave mixing in graphene optoelectronics," *Nature Photon.*, vol. 6, no. 8, pp. 554–559, Jul. 2012.

[13] X. Gan, R.-J. Shiue, Y. Gao, K. F. Mak, X. Yao, L. Li, A. Szep, D. Walker, J. Hone, T. F. Heinz, and D. Englund, "High-contrast electrooptic modulation of a photonic crystal nanocavity by electrical gating of graphene," *Nano Lett.*, vol. 13, no. 2, pp. 691–696, Feb. 2013.

[14] A. Majumdar, J. Kim, J. Vuckovic, and F. Wang, "Electrical control of silicon photonic crystal cavity by graphene," *Nano Lett.*, vol. 13, no. 2, pp. 515–518, 2013.

[15] Y. Akahane, T. Asano, B.-S. Song, and S. Noda, "Fine-tuned high-Q photonic-crystal nanocavity," *Opt. Exp.*, vol. 13, no. 4, pp. 1202–1214, 2005.

[16] X. Gan, K. F. Mak, Y. Gao, Y. You, F. Hatami, J. Hone, T. F. Heinz, and D. Englund, "Strong enhancement of light-matter interaction in graphene coupled to a photonic crystal nanocavity," *Nano Lett.*, vol. 12, no. 11, pp. 5626–5631, Oct. 2012.

[17] X. Gan, N. Pervez, I. Kymissis, F. Hatami, and D. Englund, "A high-resolution spectrometer based on a compact planar two dimensional photonic crystal cavity array," *Appl. Phys. Lett.*, vol. 100, no. 23, pp. 231104–231107, 2012.

[18] C. R. Dean, A. F. Young, I. Meric, C. Lee, L. Wang, S. Sorgenfrei, K. Watanabe, T. Taniguchi, P. Kim, K. L. Shepard, and J. Hone, "Boron nitride substrates for high-quality graphene electronics," *Nature Nanotechnol.*, vol. 5, pp. 722–726, May 2010.

[19] J. D. Joannapolous, S. G. Johnson, J. N. Winn, and R. D. Meade, *Photonic Crystals: Molding the Flow of Light*. Princeton, NJ, USA: Princeton Univ. Press, 2008.

[20] C. Manolatou, M. J. Khan, S. Fan, P. R. Villeneuve, H. A. Haus, and J. D. Joannopoulos, "Coupling of modes analysis of resonant channel add-drop filters," *IEEE J. Quantum Electron.*, vol. 35, no. 9, pp. 1322–1331, Sep. 1999.

[21] Y. Akahane, T. Asano, B.-S. Song, and S Noda, "High-Q photonic nanocavity in a two-dimensional photonic crystal," *Nature*, vol. 425, pp. 944–947, 2003.

[22] D. Englund, A. Faraon, I. Fushman, N. Stoltz, P. Petroff, and J. Vuckovic, "Controlling cavity reflectivity with a single quantum dot," *Nature*, vol. 450, no. 6, pp. 857–861, 2007.

[23] D. Englund, D. Fattal, E. Waks, G. Solomon, B. Zhang, T. Nakaoka, Y. Arakawa, Y. Yamamoto, and J. Vuckovic, "Controlling the spontaneous emission rate of single quantum dots in a two-dimensional photonic crystal," *Phys. Rev. Lett.*, vol. 95, p. 13904, Jul. 2005.

[24] C. H. Lui, K. F. Mak, J. Shan, and T. F. Heinz, "Ultrafast photoluminescence from graphene," *Phys. Rev. Lett.*, vol. 105, no. 12, pp. 127404–127407, 2010.

[25] I. Fushman, D. Englund, and J. Vučković, "Coupling of PbS quantum dots to photonic crystal cavities at room temperature," *Appl. Phys. Lett.*, vol. 87, no. 24, pp. 241102–241104, 2005.

[26] V. G. Kravets, A. N. Grigorenko, R. R. Nair, P. Blake, S. Anissimova, K. S. Novoselov, and A. K. Geim, "Spectroscopic ellipsometry of graphene and an exciton-shifted van Hove peak in absorption," *Phys. Rev. B*, vol. 81, no. 15, pp. 155413–155418, Apr. 2010.

[27] H. Li, Y. Anugrah, S. J. Koester, and M. Li, "Optical absorption in graphene integrated on silicon waveguides," *Appl. Phys. Lett.*, vol. 101, no. 11, pp. 111110–111114, 2012.

[28] F. Wang, Y. Zhang, C. Tian, C. Girit, A. Zettl, M. Crommie, and Y. R. Shen, "Gate-variable optical transitions in graphene," *Science*, vol. 320, no. 5873, pp. 206–209, Apr. 2008.

[29] Z. Q. Li, E. A. Henriksen, Z. Jiang, Z. Hao, M. C. Martin, P. Kim, H. L. Stormer, and D. N. Basov, "Dirac charge dynamics in graphene by infrared spectroscopy," *Nature Phys.*, vol. 4, no. 7, pp. 532–535, Jun. 2008.

[30] K. Mak, C. Lui, J. Shan, and T. Heinz, "Observation of an electric-field-induced band gap in bilayer graphene by infrared spectroscopy," *Phys. Rev. Lett.*, vol. 102, no. 25, pp. 100–103, 2009.

[31] N. M. R. Peres, T. Stauber, and A. H. Castro Neto, "The infrared conductivity of graphene on top of silicon oxide," *Europhys. Lett.*, vol. 84, no. 3, pp. 38002–38007, Nov. 2008.

[32] J. Gao, J. F. McMillan, M.-C. Wu, J. Zheng, S. Assefa, and C. W. Wong, "Demonstration of an air-slot mode-gap confined photonic crystal slab nanocavity with ultrasmall mode volumes," *Appl. Phys. Lett.*, vol. 96, no. 5, pp. 51123–51125, 2010.

[33] T. Ozel, A. Gaur, J. A. Rogers, and M. Shim, "Polymer electrolyte gating of carbon nanotube network transistors," *Nano Lett.*, vol. 5, no. 5, pp. 905–911, 2005.

[34] S. J. Koester and M. Li, "High-speed waveguide-coupled graphene-on-graphene optical modulators," *Appl. Phys. Lett.*, vol. 100, no. 17, pp. 171107–171110, 2012.

[35] D. A. B. Miller, "Device requirements for optical interconnects to silicon chips," *Proc. IEEE*, vol. 97, no. 7, pp. 1166–1185, Jul. 2009.

[36] G. T. Reed, G. Mashanovich, F. Y. Gardes, and D. J. Thomson, "Silicon optical modulators," *Nature Photon.*, vol. 4, no. 8, pp. 518–526, Jul. 2010.

Xuetao Gan received the B.S. degree in optical information science and technology from Northwestern Polytechnical University, Xi'an, China, in 2007. He then received the Ph.D. degree from the same university. From 2010 to 2012, he was with Englund's group as a Visiting Scholar at Columbia University. His research interests include the graphene optoelectronics and novel applications of photonic crystals.

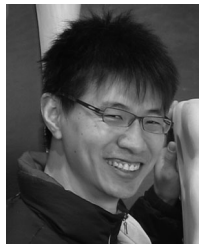

Ren-Jye Shiue received the B.S. degree in physics from National Taiwan University (NTU) in 2005. After two years of graduate study, he received the M.S. degree in electronics engineering from NTU. In 2011, he started a master's study at Columbia University and joined Englund's group. He received the M.S. degree from Columbia and moved to the Massachusetts Institute of Technology in the spring of 2013 as a Ph.D. student in the Department of Electrical Engineering and Computer Science. His research interests include the magnetotransport properties of graphene and graphene optoelectronics.

Yuanda Gao received the B.S. degree in mechanical engineering from Northeastern University, Shenyang, China, in 2009. After two years of graduate study, he received the M.S. degree in mechanical engineering from Columbia University, New York, NY, USA. In 2011, he joined Professor James Hone's group to continue his Ph.D. study at Columbia. His research interests include graphene electronics in heterostructures.

Solomon Assefa (SM'13) received the B.S. degree in physics in 2001, the B.S. degree in electrical engineering and computer science in 2001, the M.S. degree in electrical engineering and computer science in 2001, and the Ph.D. degree in 2004, all from the Massachusetts Institute of Technology. He is a Research Scientist at the IBM T.J. Watson Research Center, Yorktown Heights, NY, USA. He has worked on nanophotonics technology for optical interconnects, with responsibilities spanning research, development, and technology transfer to commercial foundry. His research contributions include high-speed optical detectors, nanostructured platforms for biosensing, and quantum information processing. He has co-authored more than 40 scientific articles, has 40 patents, and has appeared as a guest speaker at numerous conferences worldwide. Dr. Assefa is a member of the Optical Society of America and the American Physical Society. He has served as committee chair and workshop organizer for various conferences including the Optical Fibers Conference and Conference on Lasers and Electro-Optics. He is a recipient of several awards including the Technical Accomplishment Award, Corporate Recognition Award, and several Invention Achievement Awards from IBM. He was named one of the World's Top Young Innovators under 35 and received the TR35 awarded by MIT's Technology Review (2011). He was honored by the World Economic Forum as a Young Global Leader in 2013.

James Hone received the B.S. degree in physics from Yale University, New Haven, CT, USA, in 1990, and the M.S. and Ph.D. degrees in physics from the University of California, Berkeley, Berkeley, CA, USA, in 1994 and 1998, respectively. He is currently a Professor of mechanical engineering at Columbia University, New York, NY, USA. His research interests include carbon nanotubes, graphene and other layered materials, and nanobiology.

Dirk Englund received the B.S. degree in physics from Caltech in 2002. Following a year at TU Eindhoven as a Fulbright Fellow, he did his graduate studies at Stanford, and received the M.S. degree in electrical engineering and the Ph.D. in applied physics in 2008.

He was a Postdoctoral Fellow at Harvard University until 2010, when he became an Assistant Professor of electrical engineering and of applied physics at Columbia University. He moved to MIT in 2013 as Assistant Professor of electrical engineering and computer science and a member of RLE and MTL. His research focuses on quantum technologies based on semiconductor and optical systems. He received the 2012 DARPA Young Faculty Award, the 2012 IBM Faculty Award, the 2011 Presidential Early Career Award for Scientists and Engineers, the 2011 Sloan Research Fellowship in Physics, the 2008 Intelligence Community (IC) Postdoctoral Fellowship, and the 2012 IEEE-HKN Outstanding Young Professional Award.